KSME

Springer

Journal of Mechanical Science and Technology 37 (11) 2023

Original Article
DOI 10.1007/s12206-023-1010-8

Keywords:
· Ball bearing
· Local defect
· Dynamic model
· Vibration response
· Skidding

Correspondence to:
Changfeng Yan
changf_yan@163.com

Citation:
Tian, Y., Yan, C., Liu, Y., Luo, W., Kang, J., Wang, Z., Wu, L. (2023). Characteristics of vibration response of ball bearing with local defect considering skidding. Journal of Mechanical Science and Technology 37 (11) (2023) 5695~5711. http://doi.org/10.1007/s12206-023-1010-8

Received May 11th, 2023
Revised July 13th, 2023
Accepted July 17th, 2023

† Recommended by Editor
No-cheol Park

Characteristics of vibration response of ball bearing with local defect considering skidding

Yu Tian[1], Changfeng Yan[1], Yaofeng Liu[1], Wei Luo[1], Jianxiong Kang[1], Zonggang Wang[2] and Lixiao Wu[1]

[1]School of Mechanical and Electrical Engineering, Lanzhou University of Technology, Lanzhou 730050, China, [2]College of Physics & Electromechanical Engineering, Zhangye 734000, China

Abstract The occurrence and aggravation of local defects in ball bearings are closely linked to the skidding behavior of the ball. Previous studies have given less attention to investigating the impact of localized defects on the problem of bearing skidding. To investigate the dynamic response of defective bearings due to skidding, a dynamic model of the ball bearing is developed that considers various factors, including self-rotation, revolution, and radial motion of the ball, as well as the contact forces and friction forces of ball/cage and ball/race, time-varying displacement excitation, and elastohydrodynamic lubrication (EHL). Experimental signals collected from a machinery fault simulator test rig are used to validate the accuracy of the proposed model. The impact of race defects on the vibration characteristics of the bearing is analyzed, and the patterns of variation in contact and friction forces within one cycle of inner race rotation are described. The results indicate that the presence of defects intensifies the force fluctuation of the ball and causes it to deviate from its normal rolling condition. By comparing the skidding characteristics of a healthy bearing with a defective one under slippage, local defects will increase the skidding ratio of bearings. The proposed model can investigate the impact of race defects on the vibration response of ball bearings under the skidding condition.

1. Introduction

Ball bearings are crucial components of mechanical equipment, including aircraft, high-speed trains, and large generators. The dynamic performance of ball bearings significantly impacts the reliability of machines [1-3]. During the operation of bearings, skidding should not be ignored, as it can generate bearing defects and accelerate performance degradation, causing a complex vibration response [4, 5]. A dynamic model that considers skidding in defective bearings can be employed to investigate the mechanisms of vibration and the intricate coupling behavior between defects and skidding. Studying the vibration characteristics and skidding behavior of faulty bearings can be used for diagnosing faults in bearings.

Dynamic modeling is commonly employed by numerous scholars to investigate the vibration characteristics of bearings. The study of vibration mechanisms in faulty bearings contributes to understanding the generation mechanism of fault characteristics in vibration signals [1, 6-8]. Based on the race defect plane dynamic model, which mainly analyzed the translational motion of the components, Zhao et al. [9] systematically investigated the influence of the size, number, and distribution of defects on the nonlinear dynamical behavior of bearings. Liu et al. [10] suggested an improved time-varying excitation calculation method based on the dynamic model of rolling element bearings (REBs), which can be used to examine the acoustic characteristics of different defect types in the outer race. Qin et al. [11] proposed a new approach to compute displacement excitation, which can more accurately describe the impact effect of rolling elements passing through defects. Tian et al. [12, 13] utilized an established inter-shaft dynamic model to discuss the impact of rotation direction of the double rotors on the vibration properties

of faulty bearings. Ambrożkiewicz et al. [14] investigated the influence of nonlinear characteristics, such as stiffness, damping, and clearance, on the vibration response of REBs in a mathematical model of bearings with 2 Degrees of Freedom (DOFs). Khanam et al. [15] proposed an analytical model based on impact forces to explain the excitation mechanism caused by the sphere impacting the edge of the defect. Additionally, the motion characteristics of defective bearings under different lubrication states have also received attention. Luo et al. [16] explored the connection between the surface defect size of races and double-pulse features based on isothermal elastohydrodynamic lubrication (EHL). They also established an REB dynamic model with inner race spalling and further explained the double-pulse excitation mechanism. Wang et al. [17] examined influences of thermal Interaction on vibration characteristics of faulty bearings by introducing thermal EHL into the REB with a local defect.

In order to describe the dynamic behavior of REBs components more comprehensively, Gupta [18, 19] developed a representative 6 DOFs dynamic model, which is useful for studying complex dynamics problems such as cage collisions and thermal coupling. Niu et al. [20] investigated the vibration characteristics of balls passing through local defects by combining the local surface damage model with the high-speed REBs model. Cao et al. [21] studied vibration characteristics of faulty bearings by developing a dynamic model of spatial cylindrical roller bearings (CRBs) that includes multiple defect types. Jiang et al. [22] identified the shortcomings of the lumped parameter model for describing the dynamics of rolling elements and cages in bearings. They developed a comprehensive dynamic model of faulty REBs and explored the three-dimensional geometric relationship between balls and defective regions in detail. Additionally, finite element models can provide further insights into the contact relationship between bearing components [23, 24].

Most of the bearing models discussed above take into account the effects of defect excitation, contact relationship, and lubrication performance on vibration characteristics. However, in the complex motion of REBs, the pure rolling behavior of rolling elements cannot be sustained for long periods [25]. To address this issue, Harris [26] proposed an analytical method for predicting high-speed REB skidding, which effectively analyzes the impact of load and spindle speed on REB skidding. Han et al. [27] studied the slipping characteristics of CRBs under compound time-varying loading conditions and summarized the influential factors that can weaken the roller skidding ratio. The dynamic model of REB taking skidding into account was used to investigate the impact of various load states on skidding performance by Wang [28] and Oktaviana et al. [29]. Meanwhile, Tu et al. [30] constructed a skidding dynamic model of REB that describes the effect of friction force on the vibration response of roller bearings during skidding. Additionally, the skidding ratio of cage and ball has been a concern for scholars. Selvaraj et al. [31] discussed the operating parameters affecting cage skidding in CRBs using a bearing test rig. In the dynamic model of REB, Liu et al. [32] researched the flexible cage and found that it can make a more reasonable prediction of bearing skidding compared to the rigid cage. The relationship between mechanism design parameters and cage skidding was studied by Sier et al. [33] using the dynamic model of a CRB with a trilobed race. Kim [34] proposed a new method of reducing sliding in high-speed bearings by designing microscopic geometric deviations, which can help improve the bearing load recovery capacity. Gao et al. [35, 36] first proposed the concept of excessive skidding and comprehensively described the skidding behavior of rolling bearings by considering the effects of various factors such as raceway lubrication, oil temperature rise, and the forces acting on the ball and cage. Furthermore, the skidding damage of bearings is inevitable [37], and Kang et al. [38] investigated the vibration response of faulty REBs under EHL conditions, taking into account skidding influence of rolling elements. They found that the skidding of defective bearings under heavy load was less than that under light load in the low-speed phase.

As mentioned above, the study of the vibration response and skidding characteristics of REBs is critical. If only the influence of defects on the bearing vibration response mechanism is examined or only the variation pattern of bearing slippage characteristics is explored, the actual skidding behavior of the faulty bearing will be ignored. To more accurately forecast dynamic response of faulty bearings during normal service, the coupling interaction between the defect and the skidding must be considered. A dynamic model of a ball bearing containing defects and taking into account skidding behavior is proposed. The model considers the $(3N_b+5)$ DOFs of a ball bearing, including the horizontal and vertical motions of races, the rotation motion of cage, and the self-rotation, revolution, and radial motions of the ball. The variation of contact force and friction force between ball and races under EHL conditions is analyzed. The validity of model is confirmed through experimental results. The vibration response, skidding velocity, and skidding ratio of the defective bearing under skidding are compared, and the variation law of skidding characteristics of bearings is investigated.

2. Dynamic modeling of ball bearing

2.1 Model assumption

To study the vibration characteristics of defective bearings under skidding conditions, some reasonable modeling assumptions are made to reduce the complexity of calculations for the bearing system. The assumptions include the following:

1) The interaction relationship between ball and races follows Hertz contact theory, and the geometric center and mass center of the bearing component coincide.

2) The effect of temperature on bearings is neglected.

3) The bearing defect is in the early stage, and its size is smaller than the diameter of ball.

4) There is no relative displacement relationship between

outer race of ball bearing and pedestal, and the rotational characteristics of inner race and shaft remain constant.

The simplified bearing system model is depicted in Fig. 1. The mass-spring-damping system is regarded as the contact relationship between ball and races. At the same time, the contact relationship between cage and ball is reduced to a linear spring with high stiffness.

2.2 Calculation of time-varying displacement

When affected by radial loads, the inner race and ball of bearing system may experience different levels of displacement and deformation from their initial positions, which can have a significant impact on calculating the time-varying displacement of faulty bearings. Therefore, geometrical displacements and contact deformations of inner race and ball should be calculated firstly.

As shown in Fig. 2, x_i and y_i represent horizontal and vertical displacements of inner race, respectively. $\boldsymbol{r}_{bo}$ and $\boldsymbol{r}_{io}$ represent the position vectors from center of bearing to center of ball and center of inner race, respectively. $\boldsymbol{r}_{bi}$ denotes position vector from center of inner race to ball. The position of inner race in relation to ball can be calculated using Eqs. (1) and (2).

$$\boldsymbol{r}_{io} = \boldsymbol{r}_{bo} - \boldsymbol{r}_{bi} = \begin{bmatrix} x_i & y_i \end{bmatrix}^T \tag{1}$$

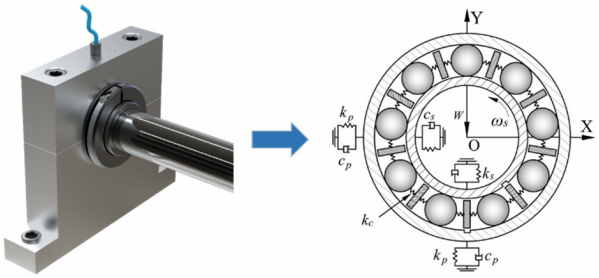

Fig. 1. Simplified model of a ball bearing.

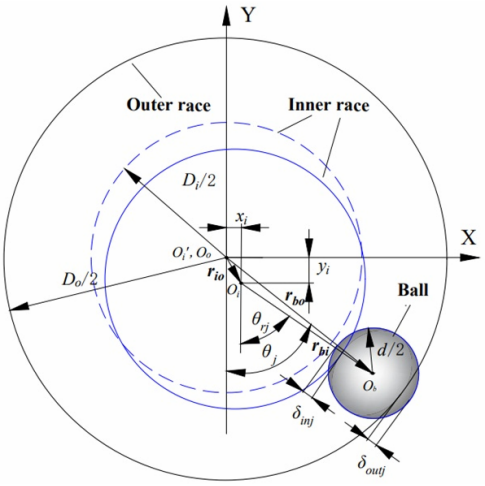

Fig. 2. Position relationship between race and ball.

$$\theta_j = \frac{2\pi(j-1)}{N_b} + \varphi_j + \theta_0 \tag{2}$$

where θ_j denotes angular position of the j-th ball relative to Y-axis, φ_j denotes revolution angle of the j-th ball, θ_0 denotes initial position angle of ball, and N_b denotes number of balls.

The contact deformation between ball and races are able to get calculated by Eq. (3) [30].

$$\begin{bmatrix} \delta_{inj} \\ \delta_{outj} \end{bmatrix} = \begin{bmatrix} 0.5(D_i + d - C_r) - r_{bi} \\ r_{bo} - 0.5(D_o - d + C_r) \end{bmatrix} \tag{3}$$

where C_r denotes radial clearance, D_i denotes diameter of inner race, D_o denotes diameter of outer race, and d denotes diameter of ball.

The overall contact deformation at the radial direction is able to be expressed by Eq. (4).

$$\delta_{ioj} = \delta_{inj} + \delta_{outj} = x_i \sin\theta_j + y_i \cos\theta_j - C_r \,. \tag{4}$$

The introduction of rectangular defects on the surface of races is intended to analyze the characteristics of ball bearings with initial defects, as shown in Fig. 3. When a ball passes through a defect, and the radial displacement varies instantaneously. In Fig. 3(a), the time-varying displacements of inner race can be represented by piece-wise functions.

$$H_i = \begin{cases} 0.5d - \sqrt{(0.5d)^2 - (l_i)^2} + 0.5D_i(1-\cos\phi_i) \\ \qquad 0 \le \left[\bmod(\theta_j, 2\pi) - \theta_0\right] \le 2\theta_i \\ 0 \qquad\qquad others \end{cases} . \tag{5}$$

Similarly, as illustrated in Fig. 3(b), time-varying displacements of ball through the defect of outer race can be expressed as Eq. (6).

$$H_o = \begin{cases} 0.5d - \sqrt{(0.5d)^2 - (l_o)^2} - 0.5D_o(1-\cos\phi_o) \\ \qquad 0 \le \left[\bmod(\theta_j, 2\pi) - \theta_0\right] \le 2\theta_o \\ 0 \qquad\qquad others \end{cases} \tag{6}$$

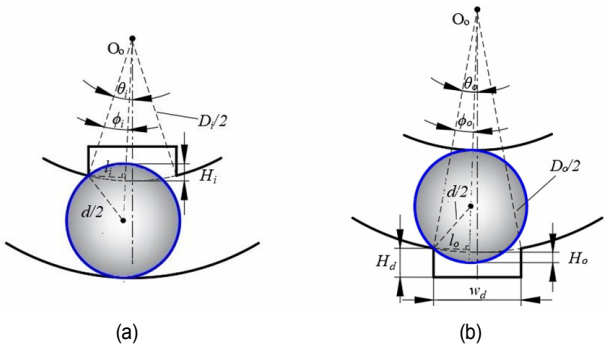

Fig. 3. Geometric position of ball and defect: (a) ball and defect of inner race; (b) ball and defect of outer race.

where ϕ_i and ϕ_o represent angles of ball entering defect of races, θ_i and θ_o represent defect angles of races, l_i and l_o represent the distances of ball entering races defects.

The specific calculation formulas are as follows.

$$\begin{bmatrix}\phi_i\\ \phi_o\end{bmatrix}=\begin{bmatrix}(\omega_s-\omega_j)t\\ \omega_j t\end{bmatrix} \tag{7}$$

$$\begin{bmatrix}\theta_i\\ \theta_o\end{bmatrix}=\begin{bmatrix}\arcsin(w_d/D_i)\\ \arcsin(w_d/D_o)\end{bmatrix} \tag{8}$$

$$\begin{bmatrix}l_i\\ l_o\end{bmatrix}=\frac{1}{2}\begin{bmatrix}D_i\sin\phi_i\\ D_o\sin\phi_o\end{bmatrix}. \tag{9}$$

The contact deformation between ball and races on faulty bearing are able to get indicated as Eq. (10).

$$\delta_{io}=(x_s-x_p)\sin\theta_j+(y_s-y_p)\cos\theta_j-C_r-H_k \tag{10}$$

where x_s and y_s are the horizontal and vertical displacements of inner race and spindle, x_p and y_p are the horizontal and vertical displacements of outer race and pedestal, respectively, *k represents i or o.*

2.3 Calculation of stiffness and damping

The contact stiffness between ball and races are able to get indicated as Eq. (11) [39].

$$\begin{bmatrix}k_i\\ k_o\end{bmatrix}=\frac{2\sqrt{2}E}{3(1-\sigma^2)}\begin{bmatrix}\delta_i^{-1.5}\sqrt{\sum\rho_i}^{-1}\\ \delta_o^{-1.5}\sqrt{\sum\rho_o}^{-1}\end{bmatrix} \tag{11}$$

where E denotes elastic modulus of ball bearing material, σ denotes Poisson's ratio, ρ_i denotes curvature of inner race, and ρ_o denotes the curvature of outer race. δ_i and δ_o denote dimensionless contact deformation of inner and outer race.

To accurately describe the stiffness, damping, and variation of the oil film in local contact zone, the internal temperature and external load of the bearing are assumed to be constant, and the lubrication is adequate. Fig. 4 illustrates the stiffness-damping model of contact zone between ball and races, considering EHL.

During normal operation of a bearing, an oil film exists between the ball and races. Using the fundamental formula of EHL [40], one can determine the minimum thickness of oil film present within the contact zone.

$$h_{\min}=3.63\bar{U}^{0.68}\bar{G}^{0.49}\bar{F}^{-0.073}(1-e^{-0.68\kappa})\bar{R} \tag{12}$$

where $\bar{R}$ denotes equivalent radius between ball and races, $\bar{U}$, $\bar{G}$ and $\bar{F}$ are all dimensionless parameters.

The total contact deformation is able to be updated as Eq. (13)

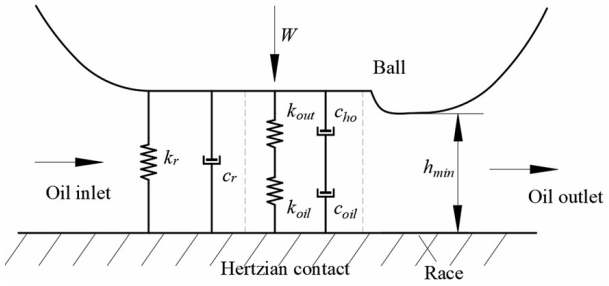

Fig. 4. Schematic of contact stiffness and damping between ball and race.

$$\delta_{io-oil}=\delta_{io}-h_{\min}. \tag{13}$$

The stiffness and damping of oil film between ball and race can be written by the equivalent Eq. (14).

$$\begin{bmatrix}k_{oil}\\ c_{oil}\end{bmatrix}=\begin{bmatrix}\mathrm{d}W/\mathrm{d}h_{\min}\\ \mathrm{d}W/\mathrm{d}u\end{bmatrix} \tag{14}$$

where W denotes radial load of ball bearing, and u denotes oil film extrusion speed.

The stiffness and damping properties of contact zone between ball and races can be expressed using Eqs. (15)-(18), which are derived from the series-parallel relation shown in Fig. 4.

$$\begin{bmatrix}k_{in-oil}\\ k_{out-oil}\end{bmatrix}=\begin{bmatrix}k_{in}k_{oil}/(k_{in}+k_{oil})+k_r\\ k_{out}k_{oil}/(k_{out}+k_{oil})+k_r\end{bmatrix} \tag{15}$$

$$K_{io-oil}=\left[1/(k_{in-oil}^{-1.5}+k_{out-oil}^{-1.5})\right]^{1.5} \tag{16}$$

$$\begin{bmatrix}c_{in-oil}\\ c_{out-oil}\end{bmatrix}=\begin{bmatrix}c_{hi}c_{oil}/(c_{hi}+c_{oil})+c_r\\ c_{ho}c_{oil}/(c_{ho}+c_{oil})+c_r\end{bmatrix} \tag{17}$$

$$C_{io-oil}=\frac{c_{in-oil}c_{out-oil}}{c_{in-oil}+c_{out-oil}} \tag{18}$$

where k_r and c_r represent stiffness and damping of oil film in inlet area, respectively, c_{hi} and c_{ho} represent the structural damping between ball and races in Hertz contact area, respectively [38, 41].

2.4 Ball/race and ball/cage interaction

The Interaction among the components of a ball bearing is intricate, as it involves multiple forces. The Hertz contact force, friction force, and oil film viscous resistance are significant forces between ball and races. Additionally, the contact force and friction force between ball and cage are also crucial forces.

2.4.1 Interaction between ball and race

The contact force between a single ball and races can be calculated using Eq. (19) [39].

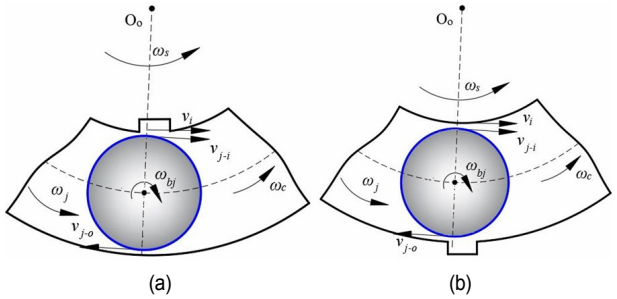

Fig. 5. Velocity relationship between ball and race when ball crosses a defect: (a) ball passing inner race with a defect; (b) ball passing outer race with a defect.

$$\begin{bmatrix} F_{inj} \\ F_{outj} \end{bmatrix} = \begin{bmatrix} k_{in-oil}\delta_{inj}^{1.5} \\ k_{out-oil}\delta_{outj}^{1.5} \end{bmatrix}. \tag{19}$$

The total contact force applied to races can be represented as Eq. (20). θ_{rj} denotes actual angular position of the j-th ball [30].

$$\begin{bmatrix} F_{io}^{\ x} \\ F_{io}^{\ y} \end{bmatrix} = \sum_{j=1}^{N_b} K_{io-oil}\delta_{io-oil}^{1.5} \begin{bmatrix} \sin\theta_{rj} \\ \cos\theta_{rj} \end{bmatrix}. \tag{20}$$

As illustrated in Fig. 5, the relative velocity relationship between ball and races on faulty bearing can be expressed by Eqs. (21) and (22).

$$\begin{bmatrix} \Delta v_{ij}^{\ i} \\ \Delta v_{oj}^{\ i} \end{bmatrix} = \begin{bmatrix} (v_{j-i}+v_{bj})-v_i \\ (v_{j-o}-v_{bj})-v_o \end{bmatrix} = \begin{bmatrix} (0.5D_i+\delta_{ioj}-H_i)\omega_j \\ (0.5D_o-H_i)\omega_j \\ +(0.5d-\delta_{inj})\omega_{bj}-(0.5D_i-H_i)\omega_s \\ -(0.5d-\delta_{outj})\omega_{bj} \end{bmatrix} \tag{21}$$

$$\begin{bmatrix} \Delta v_{ij}^{\ o} \\ \Delta v_{oj}^{\ o} \end{bmatrix} = \begin{bmatrix} (v_{j-i}+v_{bj})-v_i \\ (v_{j-o}-v_{bj})-v_o \end{bmatrix} = \begin{bmatrix} (0.5D_i+\delta_{ioj}+H_o)\omega_j \\ (0.5D_o+H_o)\omega_j \\ +(0.5d-\delta_{inj})\omega_{bj}-0.5D_i\omega_s \\ -(0.5d-\delta_{outj})\omega_{bj} \end{bmatrix} \tag{22}$$

where v_i denotes the velocity of inner race, ω_s denotes the rotational angular velocity of inner, $v_o = 0$ denotes the velocity of outer race, $v_{j\text{-}i}$ denotes velocity of ball relative to inner race, $v_{j\text{-}o}$ denotes the velocity of ball relative to outer race, v_{bj} denotes the velocity of self-rotation of ball, $\omega_j = \dot{\varphi}_j$ denotes angular velocity of revolution of ball, and $\omega_{bj} = \dot{\varphi}_{bj}$ denotes angular velocity of self-rotation of ball.

It is possible to utilize a semi-empirical formula for the computation of the friction coefficient between the components of bearing. This formula is commonly utilized in the study of the motion features of REB [30, 42].

$$\mu = (A + B|\Delta v|)\exp(-C|\Delta v|) + D \tag{23}$$

where A, B, C and D represent lubricant coefficients.

The calculation of friction force is identical for two types of faulty bearings. As an illustration, if there is a defect on inner race, it is feasible to represent the friction force between an individual ball and race by employing Eq. (24). η denotes viscosity of lubricant.

$$\begin{bmatrix} f_{inj} \\ f_{outj} \end{bmatrix} = -\mu \begin{bmatrix} F_{inj}\eta\Delta v_{ij}^{\ i}/|\Delta v_{ij}^{\ i}| \\ F_{outj}\eta\Delta v_{oj}^{\ i}/|\Delta v_{oj}^{\ i}| \end{bmatrix}. \tag{24}$$

The general formula of oil film friction force is able to be computed using as Eq. (25).

$$\begin{bmatrix} f_{io}^{\ x} \\ f_{io}^{\ y} \end{bmatrix} = \sum_{j=1}^{N_b} (f_{inj}+f_{outj}) \begin{bmatrix} \sin\theta_{rj} \\ \cos\theta_{rj} \end{bmatrix}. \tag{25}$$

2.4.2 Interaction between ball and cage

In Fig. 1, the functional relationship between the cage and ball can be simplified as a set of compressed linear springs. In this case, the spring stiffness k_c is set at 1×10^8 N/m [4, 43]. Eq. (26) is able to be employed to express contact force between a single ball and the cage.

$$F_{cj} = 0.5k_cD_m(\varphi_j - \varphi_c) \tag{26}$$

where φ_c denotes the rotation angle of cage, D_m denotes pitch diameter of bearing.

If $\varphi_j > \varphi_c$, the ball will contact the forward surface of the cage pocket. On the other hand, if $\varphi_j < \varphi_c$, the ball will come in contact with rear end face of cage pocket. The sum of contact forces of all balls applied to cage is able to be represented by Eq. (27).

$$F_c = 0.5k_cD_m\sum_{j=1}^{N_b}(\varphi_j - \varphi_c). \tag{27}$$

The relative skidding velocity of a single ball to cage can be obtained as Eq. (28).

$$\Delta v_{cj} = 0.5d\omega_{bj}. \tag{28}$$

Therefore, the total friction force between all of balls and cage can be calculated using as Eq. (29).

$$f_c = -\mu F_c\eta\Delta v_{cj}/|\Delta v_{cj}|. \tag{29}$$

2.4.3 Viscous resistance and centrifugal force of ball

The movement of ball is influenced by the viscous resistance of lubricant, which can be calculated with the help of Eq. (30) provided by Harris [39].

$$F_v = \frac{c_v\pi\xi d(D_m\dot{\varphi})^{1.95}}{32g} \tag{30}$$

where g denotes acceleration of gravity, c_v denotes drag coeffi-

cient, and ξ denotes effective fluid density of bearing.

At the same time, the centrifugal force and moment of inertia of ball about bearing center are able to be calculated using Eqs. (31) and (32).

$$F_{ce} = 0.5 m_b D_m \dot{\varphi}_j^{\ 2} \tag{31}$$

$$J_m = J_b + m_b r_{bo}^{\ 2} \tag{32}$$

where m_b denotes mass of ball, and J_b denotes rotational inertia of ball.

2.5 Dynamic equations and solutions

The dynamic equations of the proposed model are divided into three parts: 4 DOFs equations for inner and outer races, 3 DOFs equations for ball, and rotational differential equation for the cage. In the simplified model, the spindle and inner race are integrated, and the bearing pedestal and outer race are bound together. Therefore, the dynamic equations for the races can be expressed using Eq. (33).

$$\begin{cases} m_s \begin{bmatrix} \ddot{x}_s \\ \ddot{y}_s \end{bmatrix} + c_s \begin{bmatrix} \dot{x}_s \\ \dot{y}_s \end{bmatrix} + k_s \begin{bmatrix} x_s \\ y_s \end{bmatrix} = -\begin{bmatrix} f_{io}^{\ x} + F_{io}^{\ x} \\ f_{io}^{\ y} + F_{io}^{\ y} + W \end{bmatrix} \\ m_p \begin{bmatrix} \ddot{x}_p \\ \ddot{y}_p \end{bmatrix} + c_p \begin{bmatrix} \dot{x}_p \\ \dot{y}_p \end{bmatrix} + k_p \begin{bmatrix} x_p \\ y_p \end{bmatrix} = \begin{bmatrix} f_{io}^{\ x} + F_{io}^{\ x} \\ f_{io}^{\ y} + F_{io}^{\ y} \end{bmatrix} \end{cases} \tag{33}$$

where m_s, c_s, k_s represent mass, damping and stiffness of spindle and inner race, respectively, and m_p, c_p, k_p represent mass, damping, and stiffness of pedestal and outer race, respectively.

The DOFs of the ball in three directions are the primary considerations when the ball bearing is in operation. These directions include revolution around the bearing center, self-rotation, and displacement in the radial direction. The corresponding dynamic equations are presented in Eq. (34).

$$\begin{cases} J_b \ddot{\theta}_{bj} = -0.5 d (f_{inj} + f_{outj} + f_c) \\ J_m \ddot{\varphi}_j = 0.5 (f_{inj} D_i + f_{outj} D_o) - (F_c + F_v + m_b g \sin\theta_j) r_{bo} \\ m_b \ddot{r}_{bo} = F_{inj} - F_{outj} + F_{ce} + f_c + m_b g \cos\theta_j \,. \end{cases} \tag{34}$$

Furthermore, the rotation of cage around the center of bearing is able to be calculated using Eq. (35).

$$J_c \ddot{\varphi}_c = 0.5 F_c D_m \tag{35}$$

where J_c is the rotational inertia of cage [30].

3. Numerical solution and experiment equipment

3.1 Numerical solution

To compute the dynamic equations, the fourth-order Runge-Kutta integration method is utilized with a constant step size. The shaft is rotated counterclockwise as positive. The defect is located at the bottommost point of outer race, while the defect on inner race rotates along with shaft.

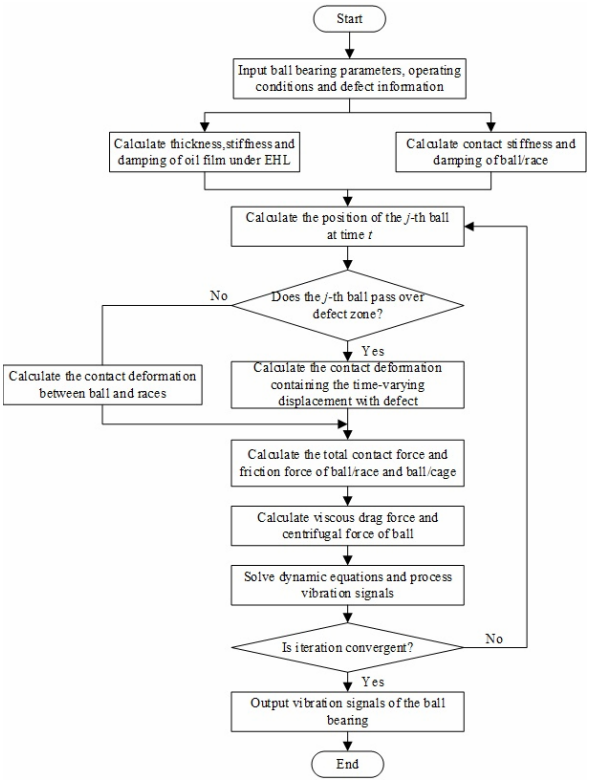

Fig. 6. Flowchart of numerical solution.

First, the program inputs the parameters, operating conditions, and defect information of the ball bearing. Then, it computes the minimum film thickness, stiffness, and damping of oil film under EHL, as well as the stiffness and damping between the ball and races. Next, it calculates time-varying displacement with defect and total time-varying displacement under EHL based on position of ball at time *t*. After that, it computes contact force and friction force between ball/races and the ball/cage. Finally, the dynamic equations of the system are resolved to derive vibration signals of bearing. The numerical solution of model uses a constant step size of 1×10^{-5} s and runs for 2 s.

3.2 Test rig

To guarantee the dependability of the suggested model, an experiment is conducted using a machinery fault simulator. The simulator is utilized to obtain vibration data from flawed ball bearings. The bearings are mounted on both ends of the spindle in Fig. 7. The faulty bearing is positioned on drive side, and the healthy bearing is positioned on far end. An acceleration sensor is mounted at the top of the pedestal, and a rotor weighing 5.1 kg is mounted in the middle of the spindle. During the experiment, a control circuit drove a 1 hp triple AC motor at a constant speed,

Table 1. Model parameters of deep groove ball bearing ER-16k.

Inner race diameter D_i (mm)	30.59
Outer race diameter D_o (mm)	46.47
Pitch diameter D_m (mm)	38.5
Diameter of ball d (mm)	7.94
Number of balls N_b	9
Radial clearance C_r (μm)	45
Contact angle α (°)	0
Mass of ball m_b (kg)	0.002
Stiffness factor of inner race k_s (N/m)	4.24×10^4
Stiffness factor of outer race k_p (N/m)	1.51×10^7
Damper factor of inner race c_s (N·s/m)	1376
Damper factor of outer race c_p (N·s/m)	2210
Elasticity modulus E (GPa)	219
Poisson ratio σ	0.3

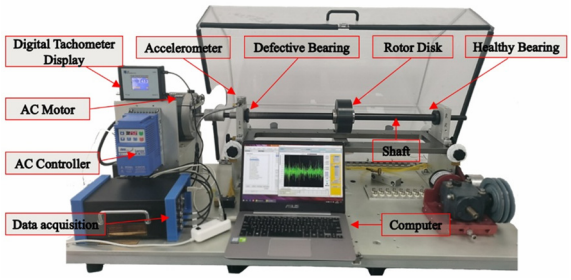

Fig. 7. Test rig of machinery fault simulator.

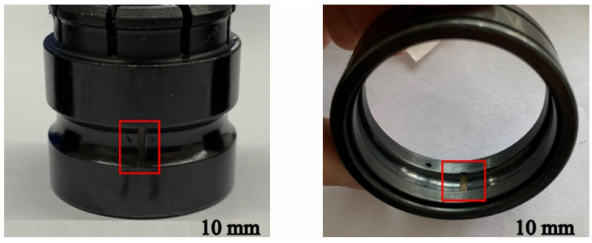

(a) (b)

Fig. 8. Experimental bearings: (a) inner race defect; (b) outer race defect.

with power transmitted via a flexible coupling connected to the spindle. To collect the vibration signals from the faulty bearings, a 16-channel portable data collector is employed. The defect width and depth of races are both identical, measuring 0.6 mm and 0.25 mm, respectively. The parameters of the sensor used in the experiment are as follows: Resonant frequency 22 kHz, sensitivity: 100 mV/g, measurement range: ±50 g, broadband resolution: 350 μg, sensing element: ceramic.

The ER-16k bearing used in the experiment features rectangular defects created through laser etching technology, as depicted in Fig. 8. While being rotated at a rate of 1600 r/min, the bearing experiences a radial load of 50 N. Vibration signals are sampled for a period of 6 s at a frequency of 15 kHz. The pertinent characteristics of the bearing are outlined in Table 1.

Table 2. Theoretical values of the rotational frequency and the fault characteristic frequency.

Speed of shaft (r/min)	f_s (Hz)	f_{bpi} (Hz)	f_{bpo} (Hz)
1600	26.67	144.8	95.25

4. Experimental results and discussions

4.1 Vibration responses of inner race or outer race with defect

The fault characteristic frequency (FCF) of RBE is a significant indicator to determine bearing fault types. When the ball rolls over defects of inner/outer race, the theoretical FCF is able to be described as Eq. (36) [8, 44].

$$f_{bpi/bpo} = \frac{N_b}{2}\left(1 \pm \frac{d}{D_m}\cos\alpha\right) f_S \tag{36}$$

where "+" represents FCF of inner race, "-" represents FCF of outer race, f_s represents spindle rotation frequency.

As illustrated in Table 2, the theoretical values of spindle rotation frequency and races FCF are able to be obtained. The experimental and simulated signals of the healthy bearing can be observed in Fig. 9. Comparing Figs. 9(a) and (c), the vibration signal of the bearing is basically stable and no high-frequency pulse signal is generated. This indicates that there is no defect in the bearing. The time domain signal is processed using the envelope method to obtain envelope spectrum, and vibration frequency of healthy bearing shows the passing frequency of the outer race. In Figs. 9(b) and (d), the corresponding harmonic frequencies can be found. The acceleration signal of a healthy bearing exhibits periodic vibrations, and the bearing vibrates at the frequency of the ball passing through a point on the outer race. This is due to the ball bearings being subjected to radial load, the number of balls in the load area to bear the load will occur in the odd and even number of constantly changing, resulting in changes to the total contact stiffness of the bearing system [39]. Additionally, the non-linear contact deformation between the ball and the race, along with the radial clearance, also influences the vibration of the system.

4.1.1 Inner race with defect

The vibration response of the inner race with a defect is presented in Fig. 10. The time interval between adjacent wave peaks is stable at approximately 6.9 ms, which is consistent with $1/f_{bpi}$, from Fig. 10(a). There is a significant difference in the peak of each wave. Furthermore, the load distribution of bearings can be classified into two zones: loaded zone and unloaded zone. The magnitude of the pulse signal generated by a defect in the inner race is significantly greater in loaded zone compared to unloaded zone. Fig. 10(c) shows the numerical simulation signals of proposed model, and the time interval of vibration signal in time domain fluctuates around

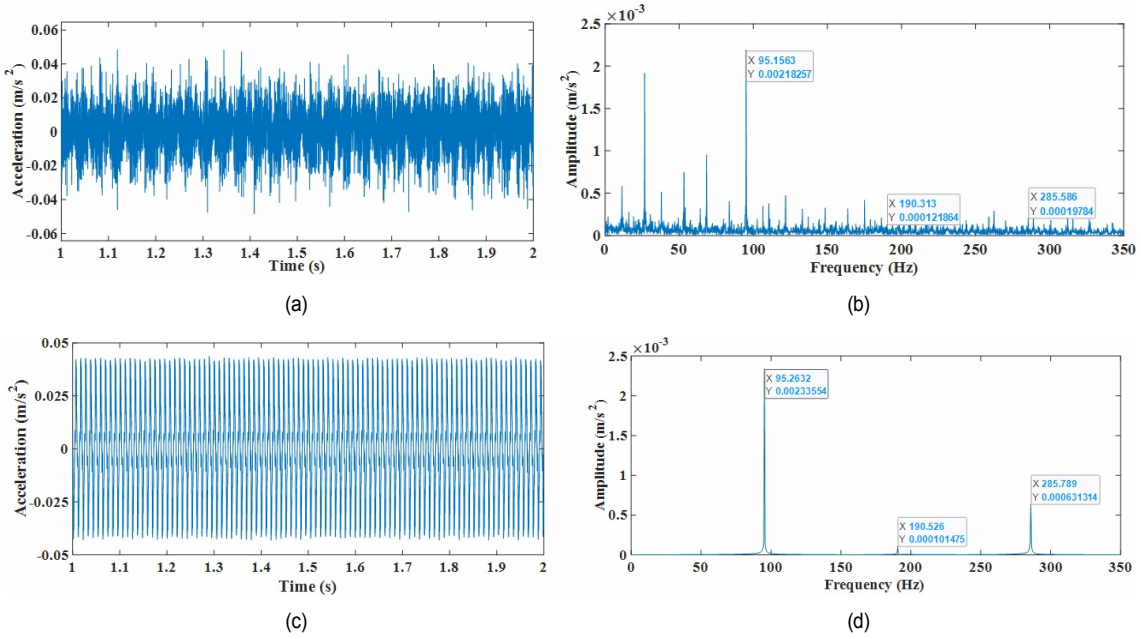

Fig. 9. Vibration response of healthy bearing: (a) experimental vibration signals; (b) envelope spectrum of (a); (c) vibration signals of proposed model; (d) envelope spectrum of (c).

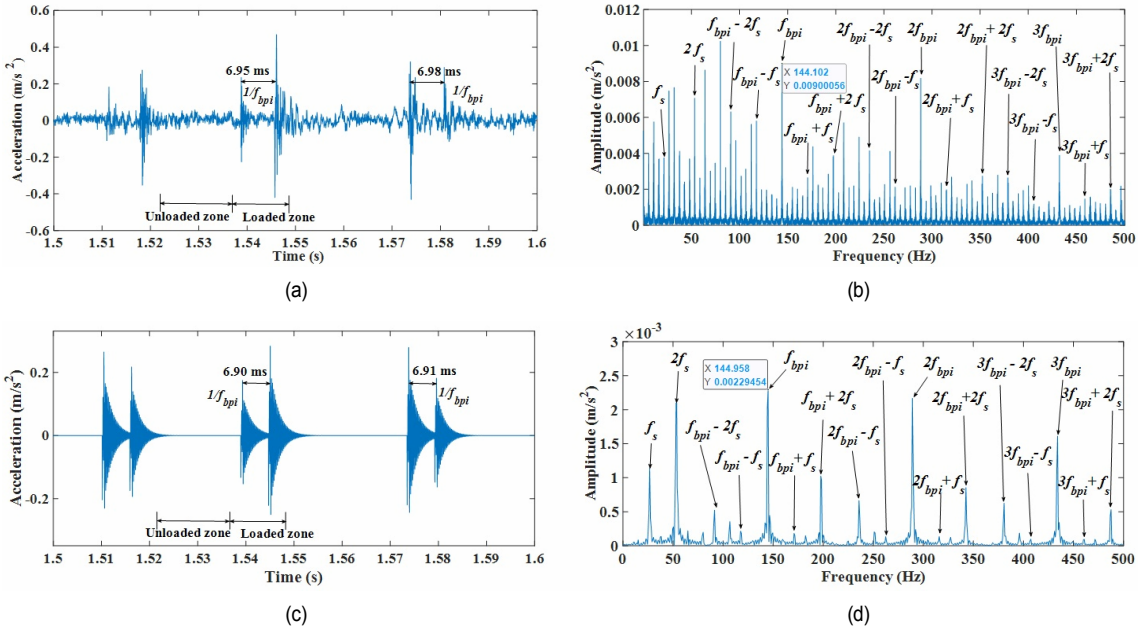

Fig. 10. Vibration response of inner race with a defect in ball bearing: (a) experimental vibration signals; (b) envelope spectrum of (a); (c) vibration signals of proposed model; (d) envelope spectrum of (c).

theoretical value, with noticeable peak fluctuations.

The envelope analysis of experimental and simulated vibration signals is presented. The frequency of f_{bpi} obtained from the experiment is 144.1 Hz, which has an error of only 0.48 % from the theoretical value of 144.8 Hz, and vibration amplitude is 0.009 m/s^2. The analysis reveals the identification of rotational frequency (f_s), inner race FCF (f_{bpi}), harmonic frequencies ($2f_s$, $2f_{bpi}$, $3f_{bpi}$), and sideband frequencies ($f_{bpi}\pm f_s$, $f_{bpi}\pm 2f_s$, $2f_{bpi}\pm f_s$, $2f_{bpi}\pm 2f_s$, $3f_{bpi}\pm f_s$, $3f_{bpi}\pm 2f_s$). The identified frequencies show that $2f_s$ is substantially larger than f_s, and the magnitude of $nf_{bpi}\pm 2f_s$ is more significant than that of $nf_{bpi}\pm f_s$.

The envelope spectrum of proposed model is indicated in Fig. 10(d), which indicates that the value of f_{bpi} is 144.95 Hz, with an error of only 0.11 % when compared to the theoretical value, and the vibration amplitude is about 0.0023 m/s^2. In addition, the harmonic and sideband frequencies can be identified and are consistent with the experimental results. Through the comparison of the results, it can be concluded that the simulation

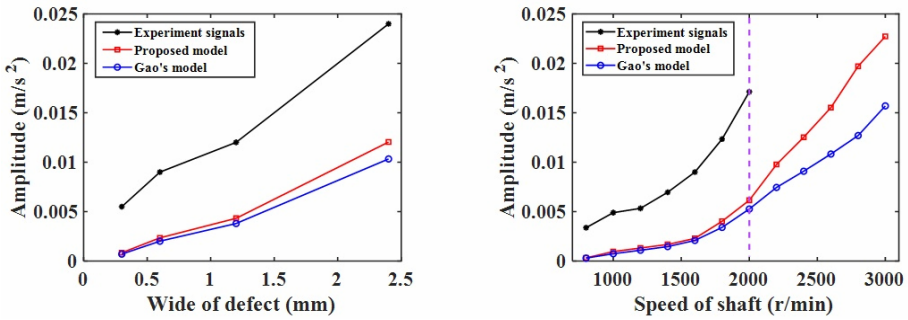

Fig. 11. Trend of amplitude change of f_{bpi} generated by inner race with defect under different working conditions: (a) different defect sizes; (b) different speed values.

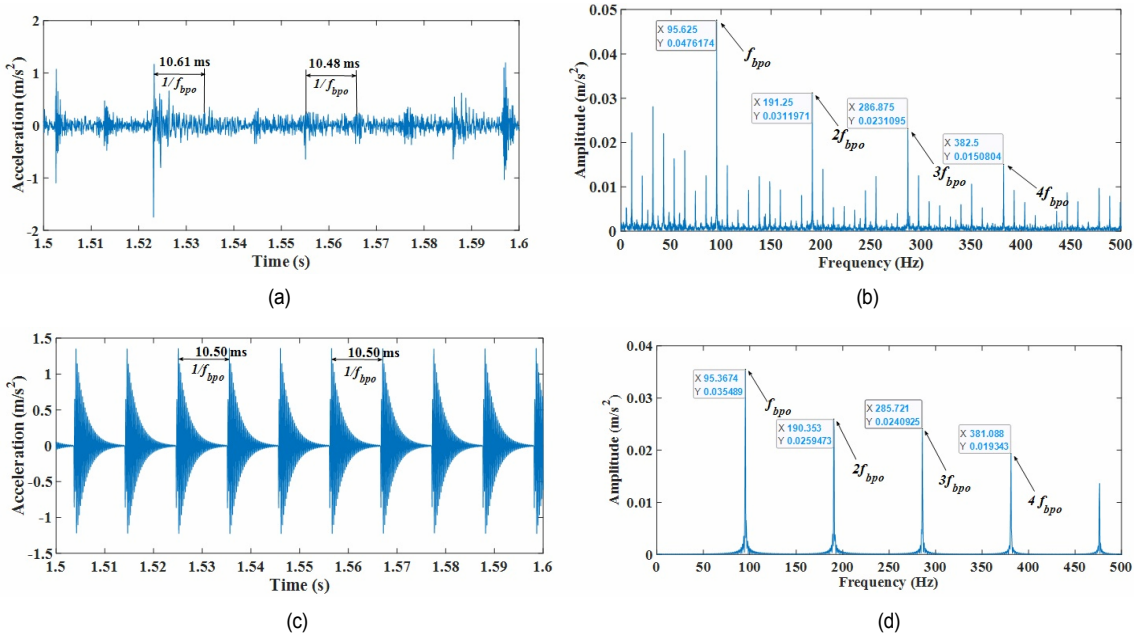

Fig. 12. Vibration response of outer race with a defect in ball bearing: (a) experimental vibration signals; (b) envelope spectrum of (a); (c) vibration signals of proposed model; (d) envelope spectrum of (c).

results of proposed model closely match experimental vibration signal, and the proposed model of inner race defect is reliable and appropriate.

The vibration amplitude of a defective bearing would change significantly when the operating conditions change. Therefore, it is essential to study the influence of various defect sizes and spindle speeds on the amplitude using experimental equipment and the established model. Fig. 11(a) illustrates the amplitude trend of the proposed inner race defect model under various working requirements. The amplitude trend of proposed model and Gao's model [41] is similar to the experimental results when the size of the inner race defect increases gradually from 0.3 mm to 2.4 mm. However, the amplitudes of Gao's model are slightly lower compared to the presented model.

The amplitude variation of f_{bpi} is depicted in Fig. 11(b) as the spindle speed is increased from 800 r/min to 3000 r/min. As the speed increases, the amplitude of the bearing failure frequency also increases. Notably, when the speed is low, the two amplitudes are similar, but the gap between them widens as the speed gradually increases. This is due to the fact that the proposed model considers the variation in friction during one cycle of bearing rotation, making it more comprehensive than the previous model, which only accounts for slip friction in the loaded zone. The abrupt rise in friction when the ball transitions from the unloaded zone to the loaded zone results in a significant increase in the radial vibration of bearing. The amplitude of proposed model is closer to experimental results compared to Gao's model, indicating the need to consider the skidding behavior between the bearing balls and the race/cage. This behavior is more representative of the actual defective bearing operation.

4.1.2 Outer race with defect

Fig. 12 presents the experimental and simulated vibration re-

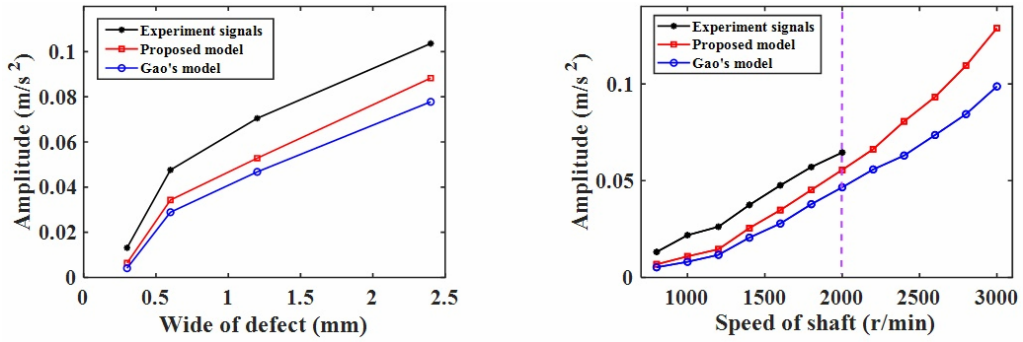

Fig. 13. Trend of amplitude of f_{bpo} under different working conditions: (a) different defect sizes; (b) different speed of shaft.

sponse results of the outer race with a defect. As illustrated in Fig. 12(a), the time-domain vibration signals obtained from the experiment indicate that the interval between two adjacent acceleration pulses fluctuates around 10.55 ms. The proposed model shows a stable time-domain pulse interval of around 10.50 ms, as shown in Fig. 12(c).

Fig. 12(b) displays the experimentally obtained acceleration signal f_{bpo} of 95.63 Hz with a vibration amplitude of approximately 0.048 m/s^2. The error between experimental value and the calculated theoretical value (95.25 Hz) is approximately 0.39 %. Harmonic frequencies ($2f_{bpo}$, $3f_{bpo}$, $4f_{bpo}$) are easily identified. Fig. 12(d) shows the envelope spectrum of vibration signals obtained from the proposed model. The vibration frequency (f_{bpo}) and harmonic frequencies can also be found. The frequency f_{bpo} is 95.36 Hz with an error of 0.16 % from the theoretical value and a vibration amplitude of 0.035 m/s^2.

Fig. 13 shows the amplitude trend of f_{bpo} for the proposed model of outer race with defects under various working conditions. Fig. 13(a) demonstrates that the amplitude growth trends of the proposed model and Gao's model are similar to the experimental results when the outer race's defect width increases from 0.3 mm to 2.4 mm. Fig. 13(b) shows the variation of f_{bpo} amplitude when the spindle speed increases from 800 r/min to 3000 r/min. As the speed increases, the amplitude of outer race fault frequency also increases. It is worth noting that the proposed model has a higher amplitude than Gao's model. This indicates that the vibration amplitude generated by the defective model of outer race, taking into account the skidding effect, is larger than that of Gao's model and closer to the experimental signals.

It is worth mentioning that in Figs. 11 and 13, the vibration amplitude of the experimental signal was measured using the test rig of the machinery fault simulator under actual operating conditions, whereas the vibration amplitude of the simulated signal was derived from the proposed model. Despite maintaining identical bearing parameters, operating conditions, and defect information for both the experiment and simulation, the simulation model is simplified based on some reasonable assumptions. Furthermore, the proposed model is formulated based on the shaft-bearing-pedestal system, which incompletely considers the impact of the rotor on vibration within the bearing-rotor system [44]. The experimental process is inevitably subject to interference from ambient noise. Therefore, there will be some differences in the vibration amplitudes obtained from the simulation and experiment.

According to the above results, the established dynamic model is in great consistency with the actual operation of the defective bearing, which provides support for further analysis of the dynamic features of defective REB under skidding.

4.2 Analysis of contact force and friction force

Skidding is a common phenomenon that occurs during the operation of ball bearings. Skidding of balls in ball bearings is mainly caused by the significant change in contact force between the balls and inner race due to centrifugal force. This causes a decrease in friction force between balls and inner race, making it insufficient to overcome the viscous resistance of lubricant and the resistance of the cage. High speed and light loads exacerbate the skidding phenomenon in ball bearings. Therefore, it is beneficial to analyze the contact force and friction force in ball bearings with local defects. To investigate this, the bearing speed is set to 2000 r/min and the radial load to 200 N, while maintaining a defect size consistent with the experimental bearing. The study compares the changes in contact force and friction force between healthy and faulty bearings.

The contact force between ball and races in a healthy bearing is indicated in Fig. 14(a) to have cyclic changes. The radial load causes the ball bearing to be divided into loaded and non-loaded zones [39]. In the loaded zone, the contact force between the ball and races increases dramatically, reaching a peak at the bottom of the ball bearing. At this point, the outer race has a greater contact force than the inner race. In the non-load zone, the centrifugal force causes the ball to contact the outer race, reducing the contact force between the ball and inner race to zero, while the outer race contact force fluctuates.

The defect on the inner race rotates with the spindle, and its impact position with the ball is not fixed. Fig. 14(c) intercepts

the contact force variation for two cycles of inner race rotation, indicating significant fluctuations in contact force occur when the ball passes through the defect. At this point, the contact force on the inner race briefly exceeds that on the outer race, and this fluctuation is transmitted and affects the change in contact force after the impact. This is because the ball crashes into the trailing edge of the defect [16], generating an impact force that continues for some time until the energy is dissipated. The impact force on the inner race is greater than that on the outer race.

The defect on outer race is located at the bottom of the ball bearing and is stationary. The position where the ball rolls over the defect and the location of the contact force mutation remain fixed. As shown in Fig. 14(e), the contact force on outer race is consistently greater than that on inner race. As the ball reaches the point of maximum load in the bearing, the contact force on the outer race experiences a significant variation, leading to significant fluctuations in the contact force throughout the loaded zone when compared to a healthy bearing.

The friction of the race is primarily influenced by the time-dependent friction coefficient and contact force. The time-dependent friction coefficient is correlated with the relative skidding speed. In Fig. 14(b), the variation of the friction between ball and races is divided into four phases. In phase 1, when a ball enters the loaded zone, the friction force between ball and races increases rapidly. The friction force on the inner race is slightly less than that on outer race due to the surge of contact load. In phase 2, firstly, the friction force on the outer race reaches a peak and then starts to decrease. The friction force on the inner race continues to grow for a while and then reaches a peak. At this point, the friction force on the inner race is significantly larger than that on the outer race. The difference in the friction force on inner and outer races is due to the influence of skidding velocity, which is explained in Fig. 15(a). In phase 3, the contact force gradually decreases, and the friction force of the race decreases accordingly. In phase 4, as the ball enters the unloaded zone, the friction force on the inner race rapidly decreases to near 0 N, and the friction force on outer race fluctuates slightly above 0 N.

Fig. 14(d) illustrates that a defect on inner race would lead to a violent oscillation of the friction force on inner race, while the friction force on the outer race is not significantly affected. As

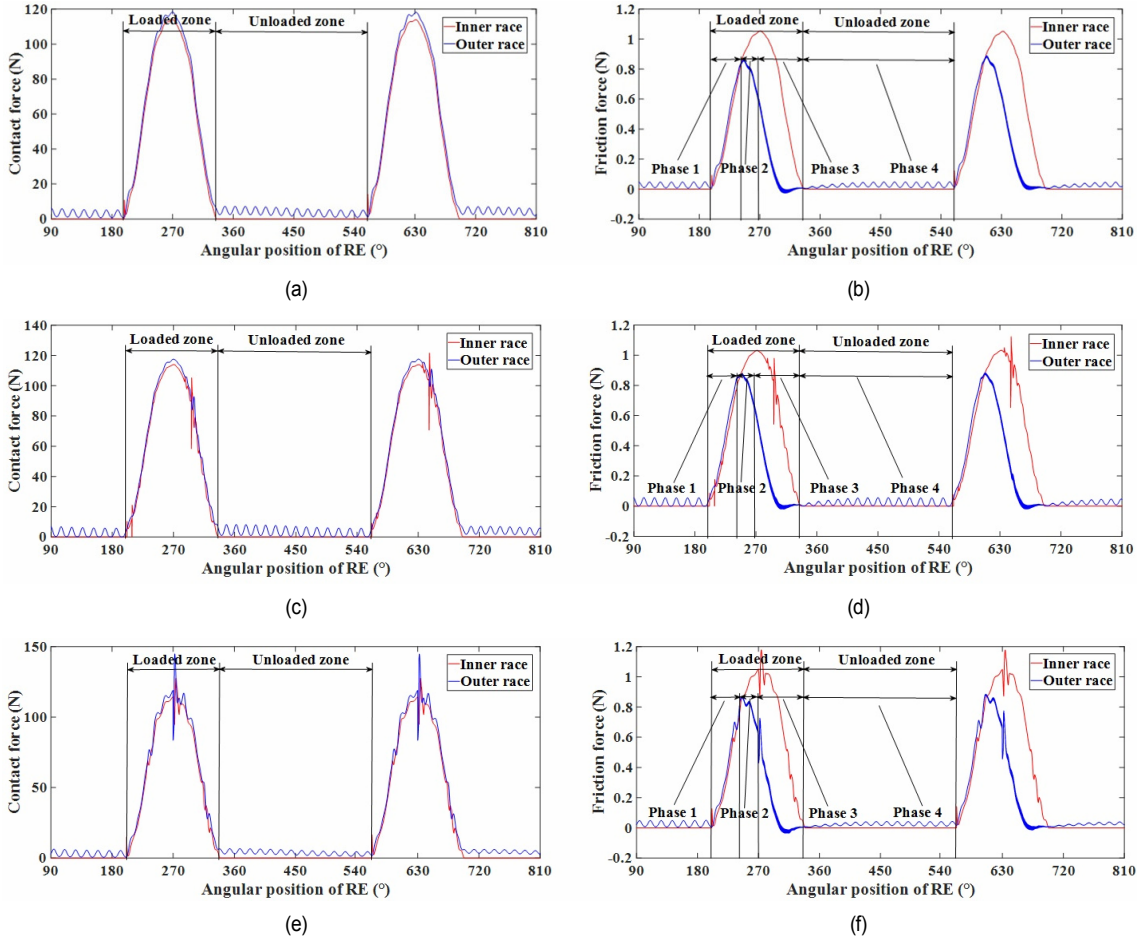

Fig. 14. Comparison of contact force and friction force: (a) contact force of healthy bearing; (b) friction force of healthy bearing; (c) contact force on inner race with a defect; (d) friction force on inner race with a defect; (e) contact force on outer race with a defect; (f) friction force on outer race with a defect.

depicted in Fig. 14(f), a defect on the outer race impacts the friction forces on both the inner and outer races. Such fluctuations can be observed in the loaded zone. Based on the above phenomena, it can be found that bearing race defects will increase the instability of contact force and friction force.

4.3 Analysis of skidding characteristics

The skidding ratio plays a crucial role in determining whether skidding will occur in a ball bearing and the severity of its behavior. In a pure rolling state, the theoretical speed of ball and cage are able to be computed as shown in previous studies [31, 45]. The skidding ratio of the ball and cage can be expressed mathematically using Eqs. (37) and (38).

$$S_b = \frac{\omega_{bt} - \dot{\theta}_j}{\omega_{bt}} \times 100\% \tag{37}$$

$$S_c = \frac{\omega_{ct} - \dot{\theta}_c}{\omega_{ct}} \times 100\% \tag{38}$$

where ω_{bt} and ω_{ct} represent the theoretical rotational speed of ball and cage.

The bearing conditions used in this section are consistent with those described in Sec. 4.2. Fig. 15(a) illustrates the skidding velocity of inner and outer races of a healthy bearing. The skidding velocity undergoes three distinct phases in the loaded zone. In phase 1, a rapid decline in skidding velocity occurs. In phase 2, the outer race experiences a greater decrease in skidding velocity compared to the inner race. In phase 3, the skidding velocity transitions from a smooth to a lifted state due to a decrease in contact force. Phase 4 is the unloaded zone, where the skidding velocity of inner and outer races increases rapidly.

Figs. 15(c) and (e) illustrate that the skidding velocity of a faulty bearing follows the same pattern as that of a healthy bearing. The skidding velocity of the defective bearing exhibits fluctuations in phase 4. The faulty bearing has a higher skidding velocity than the healthy bearing, and the inner race has a higher skidding velocity than the outer race. Fig. 15(b) shows that the skidding ratios of the ball and cage in a healthy bearing

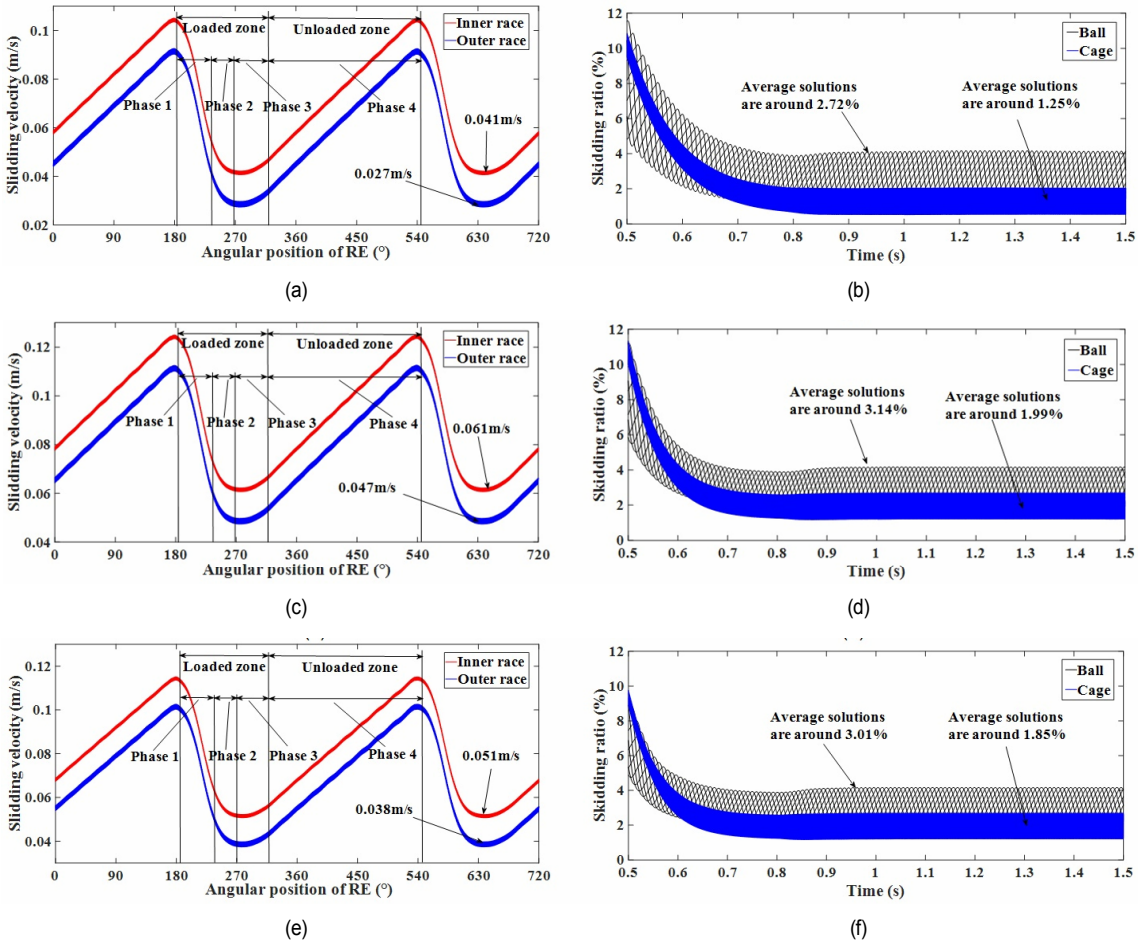

Fig. 15. Comparison of skidding velocity and skidding ratio: (a) skidding velocity of healthy bearing; (b) skidding ratio of healthy bearing; (c) skidding velocity of inner race with a defect; (d) skidding ratio of inner race with a defect; (e) skidding velocity of outer race with a defect; (f) skidding ratio of outer race with a defect.

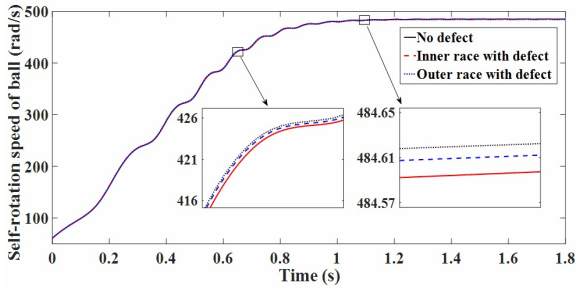

Fig. 16. Comparison of self-rotation speed of ball.

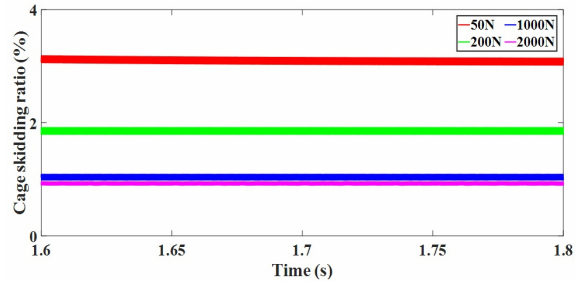

(a)

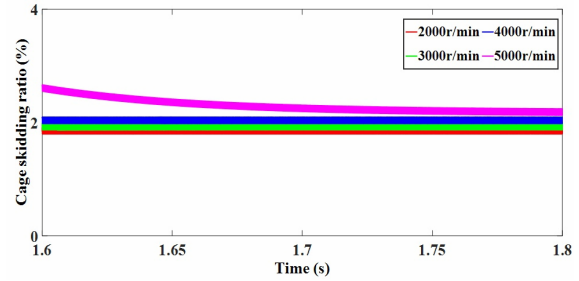

(b)

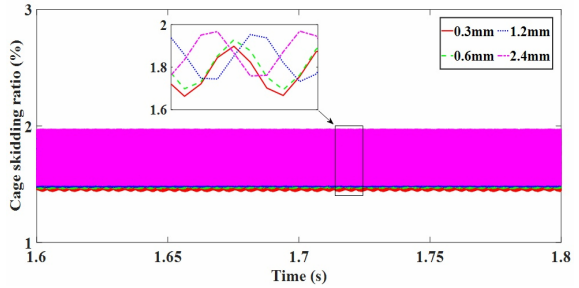

(c)

Fig. 17. Cage skidding ratio of inner race with defect under different working conditions: (a) different radial load; (b) different spindle speed; (c) different defect sizes.

are 2.72 % and 1.25 %, respectively. Comparing Fig. 15(d) with Fig. 15(f), it is apparent that local defects in the ball bearing lead to an increased skidding ratio. The presence of defects on inner race has a greater effect on skidding than the presence of defects on outer race. This is primarily because the collision position between the inner raceway defect and the ball is unpredictable, and the relative velocity difference between them varies considerably.

The self-rotation speed of ball can be illustrated in Fig. 16. Although there is no significant difference between the rising speed trend of healthy and faulty bearings, the enlarged view in Fig. 16 shows that healthy bearings have a higher self-rotation speed compared to faulty bearings, and defective inner races have the slowest speed. Fig. 17 investigates the effects of varying radial loads, spindle speeds, and defect sizes on the cage skidding ratio using a skidding model of inner race defects. For inner race speeds of 2000 r/min, radial loads of 50 N, 200 N, 1000 N, and 2000 N are applied to the ball bearing, and the resulting trends of cage skidding ratio with time are shown in Fig. 17(a). A significant decrease in cage skidding ratio is observed as the radial load increases. Light loads are able to cause severe skidding behavior on faulty bearings.

The radial load of ball bearing is set at 200 N, and the spindle speed is varied between 2000 r/min, 3000 r/min, 4000 r/min, and 5000 r/min. Fig. 17(b) shows that higher spindle speeds can lead to an increase in cage skidding ratio, resulting in severe skidding. Fig. 17(c) illustrates that when the bearing is loaded with a radial force of 200 N and an inner race speed of 2000 r/min, the defect width expands from 0.3 mm to 2.4 mm. It can be observed from enlarged view that the larger defect sizes will have a higher cage skidding ratio. By comparing Figs. 17(a)-(c), it is evident that spindle speed and load have the most significant impact on the stability of skidding ratio, while the size of the defect has a negligible effect. This implies that controlling skidding behavior for defective bearings should consider the impact of both speed and load.

5. Conclusions

A dynamic model of defective ball bearing is proposed, which considers the skidding effect, contact force, friction force, time-varying displacement excitation and isothermal EHL. The proposed model is compared with experimental results to validate its reliability. The model can be useful for studying vibration response and skidding characteristics of bearings with localized defects. The main conclusions are as follows:

1) The proposed model considering the skidding behavior of ball/cage and ball/race is compared with Gao's model to verify the correctness of the model. It is also found that the FCF of defective bearing increases with the increase of speed or defect size, and the proposed model is closer to the experimental results.

2) Comparing the defect model of the bearing with the health model, defects on race can produce fluctuating and violent acting forces on the bearing. The skidding behavior exacerbates the change in contact force and friction force between ball and the defective race.

3) Defect can cause an increase in skidding velocity and skidding ratios of ball and cage. Cage skidding ratio can be affected by the rotation speed of ball bearing, radial load and defect size. Low spindle speeds and heavy loads can effectively reduce the skidding behavior of defective bearings.

Acknowledgments

This work is supported by the National Natural Science Foundation of China (Grant nos.51765034), the Excellent Doctoral Program in Gansu Province (Project no. 22JR5RA230) and the Excellent Graduate Student "Innovation Star" project of Education Department of Gansu Province (Project no. 2023 CXZX-409).

Nomenclature

A : Lubricant coefficients
B : Lubricant coefficients
c_v : Drag coefficient
c_h : Damping coefficient
c_{oil} : Damping of oil film between ball and races
c_r : Damping of oil film in the inlet area
c_{hi}, c_{ho} : Structural damping between ball and races
$c_{in\text{-}oil}$, $c_{out\text{-}oil}$: Damping of oil film and races
$c_{io\text{-}oil}$: Total damping under EHL
c_s : Damping of spindle and inner race
c_p : Damping of pedestal and outer race
C_r : Radial clearance of bearing
C : Lubricant coefficient
d : Diameter of ball
D : Lubricant coefficient
D_m : Pitch diameter of ball bearing
D_i : Inner race diameter
D_o : Outer race diameter
E : Elastic modulus of ball bearing material
f_c : Total friction force between all balls and cage
f_{inj}, f_{outj} : Friction force between a single ball and races
f_{io}^{x} : Total oil film friction force of x-direction
f_{io}^{y} : Total oil film friction force of y-direction
f_s : Spindle rotation frequency
f_{bpi} : Fault characteristic frequency of inner race
f_{bpo} : Fault characteristic frequency of outer race
F_{cj} : Contact force between a single ball and cage
F_c : Sum of contact forces of all balls and cage
F_v : Viscous resistance
F_{ce} : Centrifugal force
F_{inj}, F_{outj} : Contact force between a single ball and races
F_{io}^{x} : Total contact force applied to races of x-direction
F_{io}^{y} : Total contact force applied to races of y-direction
$\bar{F}$: Dimensionless material parameter
g : Acceleration of gravity
$\bar{G}$: Dimensionless load parameter
h_{min} : Minimum thickness of oil film
H_i, H_o : Time-varying displacement function
H_d : Defect depth
J_b : Rotational inertia of ball
J_c : Rotational inertia of cage
J_m : Moment of inertia of ball about ball bearing axis
k_s : Stiffness of spindle and inner race
k_c : Spring stiffness
k_p : Stiffness of pedestal and outer race
k_{oil} : Stiffness of oil film between ball and races
$k_{io\text{-}oil}$: Total stiffness under EHL
$k_{in\text{-}oil}$, $k_{out\text{-}oil}$: Stiffness of oil film and races
k_i, k_o : Contact stiffness between ball and races
l_i, l_o : Distances of ball entering races defect
m_s : Mass of spindle and inner race
m_p : Mass of pedestal and outer race
N_b : Number of balls
r_{bo} : Position vectors from center of bearing to of ball
r_{io} : Position vectors from center of bearing to center of inner race
r_{bi} : Position vector from center of inner race to ball
$\bar{R}$: Equivalent radius between ball and races
S_b : Ball skidding ratio
S_c : Cage skidding ratio
u : Oil film extrusion speed
$\bar{U}$: Dimensionless velocity parameter
v_i : Velocity of inner race
$v_{j\text{-}i}$: Velocity of revolution of ball relative to inner race
$v_{j\text{-}o}$: Velocity of revolution of ball relative to outer race
v_{bj} : Velocity of self-rotation of ball
v_{cj} : Relative skidding velocity of a single ball to cage
v_{iji}, v_{ijo} : Relative velocity between ball and inner race
v_{oji}, v_{ojo} : Relative velocity between ball and outer race
W : Radial load of ball bearing
W_d : Defect width
x_i, y_i : Horizontal and vertical displacements of inner race
x_s, y_s : Horizontal and vertical displacements of inner race and spindle
x_p, y_p : Horizontal and vertical displacements of outer race and bearing pedestal
α : Contact angle
δ_{io} : Contact deformation between ball and races with a defect
$\delta_{io\text{-}oil}$: Total contact deformation under EHL
δ_{ioj} : Total contact deformation between ball and races
δ_{inj}, δ_{out} : Contact deformation between ball and races
η : Viscosity of the lubricant
θ_j : Angular position of the j-th ball
θ_0 : Initial position angle of ball
θ_i, θ_o : Defect angles of races
θ_{rj} : Actual angular position of the j-th ball
μ : Friction coefficient
ξ : Effective fluid density of ball bearing.
ρ_i, ρ_o : Sum of the curvature of inner and outer race
σ : Poisson's ratio
φ_{bj} : Angular of self-rotation of ball
φ_j : Revolution angle of the j-th ball
φ_c : Rotation angle of cage
ϕ_i, ϕ_o : Angles of the ball entering race defects
ω_s : Rotational angular velocity of inner
ω_j : Angular velocity of revolution of ball
ω_{bj} : Angular velocity of self-rotation of ball
ω_{bt} : Theoretical rotational speed of ball
ω_{ct} : Theoretical rotational speed of cage

References

[1] H. Cao, L. Niu, S. Xi and X. Chen, Mechanical model development of rolling bearing-rotor systems: A review, *Mechanical Systems and Signal Processing*, 102 (2018) 37-58.

[2] J. Liu and Y. Shao, Overview of dynamic modelling and analysis of rolling element bearings with localized and distributed faults, *Nonlinear Dynamics*, 93 (4) (2018) 1765-1798.

[3] Z. Jin, Y. Xiao, D. He, Z. Wei, Y. Sun and W. Yang, Fault diagnosis of bearing based on refined piecewise composite multivariate multiscale fuzzy entropy, *Digital Signal Processing*, 133 (2023) 103884.

[4] Q. Han and F. Chu, Nonlinear dynamic model for skidding behavior of angular contact ball bearings, *Journal of Sound and Vibration*, 354 (2015) 219-235.

[5] S. Gao, Q. Han, P. Pennacchi, S. Chatterton and F. Chu, Dynamic, thermal, and vibrational analysis of ball bearings with over-skidding behavior, *Friction*, 11 (4) (2022) 580-601.

[6] J. Liu, L. Wang and Z. Shi, Dynamic modelling of the defect extension and appearance in a cylindrical roller bearing, *Mechanical Systems and Signal Processing*, 173 (2022) 109040.

[7] Y. Liu, C. Yan, J. Kang, Z. Wang and L. Wu, Investigation on characteristics of vibration interaction between supporting bearings in rotor-bearing system, *Measurement*, 216 (2023) 113000.

[8] W. Smith and R. Randall, Rolling element bearing diagnostics using the case western reserve university data: A benchmark study, *Mechanical Systems and Signal Processing*, 64 (2015) 100-131.

[9] Z. Zhao, X. Yin and W. Wang, Effect of the raceway defects on the nonlinear dynamic behavior of rolling bearing, *Journal of Mechanical Science and Technology*, 33 (6) (2019) 2511-2525.

[10] J. Liu, Y. Xu and G. Pan, A combined acoustic and dynamic model of a defective ball bearing, *Journal of Sound and Vibration*, 501 (2021) 116029.

[11] Y. Qin, F. Cao, Y. Wang, W. Chen and H. Chen, Dynamics modelling for deep groove ball bearings with local faults based on coupled and segmented displacement excitation, *Journal of Sound and Vibration*, 447 (2019) 1-19.

[12] J. Tian, Y. Ai, C. Fei, F. Zhang and Y. Choy, Dynamic modeling and simulation of inter-shaft bearings with localized defects excited by time-varying displacement, *Journal of Vibration and Control*, 25 (8) (2019) 1436-1446.

[13] C. Wang, J. Tian, F. Zhang, Y. Ai and Z. Wang, Dynamic modeling and simulation analysis of inter-shaft bearing fault of a dual-rotor system, *Mechanical Systems and Signal Processing*, 193 (2023) 110260.

[14] B. Ambrożkiewicz, G. Litak, A. Georgiadis, N. Meier and A. Gassner, Analysis of dynamic response of a two degrees of freedom (2-DOF) ball bearing nonlinear model, *Applied Sciences*, 11 (2) (2021) 787-787.

[15] S. Khanam, J. K. Dutt and N. Tandon, Impact force based model for bearing local fault identification, *Journal of Vibration and Acoustics*, 137 (5) (2015) 1-13.

[16] M. Luo, Y. Guo, H. Andre, X. Wu and J. Na, Dynamic modeling and quantitative diagnosis for dual-impulse behavior of rolling element bearing with a spall on inner race, *Mechanical Systems and Signal Processing*, 158 (2021) 107711.

[17] Y. Wang, C. Yan, Z. Lu, Y. Liu and L. Wu, Effect of thermal elastohydrodynamic lubrication on vibration characteristics of ball bearing with local defect, *Proceedings of the Institution of Mechanical Engineers, Part K: Journal of Multi-body Dynamics*, 236 (3) (2022) 488-500.

[18] P. Gupta, Dynamics of rolling-element bearings—part III: ball bearing analysis, *Journal of Lubrication Technology*, 101 (3) (1979) 312-318.

[19] P. Gupta and H. Gibson, Real-time dynamics modeling of cryogenic ball bearings with thermal coupling, *Journal of Tribology*, 143 (3) (2021) 031201.

[20] L. Niu, H. Cao, Z. He and Y. Li, Dynamic modeling and vibration response simulation for high speed rolling ball bearings with localized surface defects in raceways, *Journal of Manufacturing Science and Engineering*, 136 (4) (2014) 041015.

[21] H. Cao, S. Su, X. Jing and D. Li, Vibration mechanism analysis for cylindrical roller bearings with single/multi defects and compound faults, *Mechanical Systems and Signal Processing*, 144 (C) (2020) 106903.

[22] Y. Jiang, W. Huang, W. Wang and G. Peng, A complete dynamics model of defective bearings considering the three-dimensional defect area and the spherical cage pocket, *Mechanical Systems and Signal Processing*, 185 (2023) 109743.

[23] F. Shen and K. Zhou, An elasto-plastic-damage model for initiation and propagation of spalling in rolling bearings, *International Journal of Mechanical Sciences*, 161-162 (C) (2019) 105058.

[24] Y. Yang, W. Yang and D. Jiang, Simulation and experimental analysis of rolling element bearing fault in rotor-bearing-casing system, *Engineering Failure Analysis*, 92 (2018) 205-221.

[25] W. Tu, Y. Luo, W. Yu and Y. Yu, Investigation of the dynamic local skidding behaviour of rollers in cylindrical roller bearings, *Proceedings of the Institution of Mechanical Engineers, Part K: Journal of Multi-body Dynamics*, 233 (4) (2019) 899–909.

[26] T. A. Harris, An analytical method to predict skidding in high speed roller bearings, *ASLE Transactions*, 9 (3) (2008) 229-241.

[27] Q. Han, X. Li and F. Chu, Skidding behavior of cylindrical roller bearings under time-variable load conditions, *International Journal of Mechanical Sciences*, 135 (2018) 203–214.

[28] Y. Wang, W. Wang, S. Zhang and Z. Zhao, Investigation of skidding in angular contact ball bearings under high speed, *Tribology International*, 92 (2015) 404-417.

[29] L. Oktaviana, V. Tong and S. Hong, Skidding analysis of angular contact ball bearing subjected to radial load and angular misalignment, *Journal of Mechanical Science and Technology*, 33 (2) (2019) 837-845.

[30] W. Tu, W. Yu, Y. Shao and Y. Yu, A nonlinear dynamic vibration model of cylindrical roller bearing considering skidding, *Nonlinear Dynamics*, 103 (3) (2021) 2299-2313.

[31] A. Selvaraj and R. Marappan, Experimental analysis of factors influencing the cage slip in cylindrical roller bearing, *The Inter-*

national Journal of Advanced Manufacturing Technology, 53 (5) (2011) 635-644.
[32] Y. Liu, Z. Chen, L. Tang and W. Zhai, Skidding dynamic performance of rolling bearing with cage flexibility under accelerating conditions, *Mechanical Systems and Signal Processing*, 150 (2021) 107257.
[33] D. Sier, Y. Lu, W. Zhang, X. Sun and Z. Lu, Cage slip characteristics of a cylindrical roller bearing with a trilobe-raceway, *Chinese Journal of Aeronautics*, 31 (2) (2018) 351-362.
[34] S. Kim, Micro-geometry deviation to reduce the cage slip of high-speed cylindrical roller bearings, *Journal of Mechanical Science and Technology*, 37 (2) (2023) 595-605.
[35] S. Gao, S. Chatterton, P. Paolo, Q. Han and F. Chu, Skidding and cage whirling of angular contact ball bearings: Kinematic-hertzian contact-thermal-elasto-hydrodynamic model with thermal expansion and experimental validation, *Mechanical Systems and Signal Processing*, 166 (2022) 108427.
[36] S. Gao, S. Chatterton, N. Lorenzo and P. Paolo, Ball bearing skidding and over-skidding in large-scale angular contact ball bearings: Nonlinear dynamic model with thermal effects and experimental results, *Mechanical Systems and Signal Processing*, 147 (2021) 107120.
[37] X. Xie, J. Xu and J. Luo, Analysis of skid damage to cylindrical roller bearing of mainshaft of aeroengine, *Journal of Mechanical Science and Technology*, 34 (8) (2020) 3239-3247.
[38] J. Kang, Y. Lu, Y. Zhang, C. Liu, S. Li and N. Mueller, Investigation on the skidding dynamic response of rolling bearing with local defect under elastohydrodynamic lubrication, *Mechanics and Industry*, 20 (6) (2019) 615.
[39] T. A. Harris and M. N. Kotzalas, *Concepts of Bearing Technology*, 5nd Ed., CRC Press, Taylor and Francis (2006).
[40] B. J. Hamrock and D. Dowson, Isothermal elastohydrodynamic lubrication of point contacts: part III—fully flooded results, *Journal of Lubrication Technology*, 99 (2) (1977) 159-171.
[41] X. Gao, C. Yan, Y. Liu, P. Yan, J. Yang and L. Wu, A 4-DOF dynamic model for ball bearing with multiple defects on raceways, *Proceedings of the Institution of Mechanical Engineers, Part K: Journal of Multi-body Dynamics*, 235 (1) (2021) 3-18.
[42] W. Zhang, S. Deng, G. Chen and Y. Cui, Study on the impact of roller convexity excursion of high-speed cylindrical roller bearing on roller's dynamic characteristics, *Mechanism and Machine Theory*, 103 (2016) 21-39.
[43] W. Tu, Y. Shao and C. K. Mechefske, An analytical model to investigate skidding in rolling element bearings during acceleration, *Journal of Mechanical Science and Technology*, 26 (8) (2012) 2451-2458.
[44] W. Luo, C. Yan, Y. Liu, Z. Wang, Y. Tian and L. Wu, Dynamic response of rolling element bearing with compound fault considering defect-rolling-element interaction, *Proceedings of the Institution of Mechanical Engineers, Part C: Journal of Mechanical Engineering Science* (2023).
[45] A. P. Patil, B. K. Mishra and S. P. Harsha, Raceway defect analysis of rolling element bearing for detecting slip and correlating the force on rolling element with peak acceleration due to impact, *Measurement*, 179 (2021) 109394.

Yu Tian is currently a master student in the School of Mechanical and Electrical Engineering at Lanzhou University of Technology, China. His research interests include dynamic modeling of rolling bearings and fault diagnosis.

Changfeng Yan received his Ph.D. degree from Tongji University, China, in 2010. He is currently a Professor in the School of Mechanical and Electrical Engineering at Lanzhou University of Technology, doctoral supervisor, China. His research interests include fault diagnosis and signal process.

Yaofeng Liu received his M.S. degree from the School of Mechanical and Electrical Engineering, Lanzhou University of Technology, China, in 2020. He is currently pursuing a Ph.D. degree with the School of Mechanical and Electrical Engineering at Lanzhou University of Technology. His research interests include rotor-bearing dynamic models and fault diagnosis.

Wei Luo received his M.S. degree from the School of Mechanical and Electrical Engineering, Lanzhou University of Technology, China, in 2023. His research interests include dynamic modeling of rolling bearings and fault diagnosis.

Jianxiong Kang received his Ph.D. degree from the School of Mechanical and Precision Instrument Engineering, Xi'an University of Technology, China, in 2022. He is currently a lecturer in the School of Mechanical and Electrical Engineering at the Lanzhou University of Technology, master supervisor, China. His research interests include dynamic modeling and health management.

Zonggang Wang received his M.S. degree from the College of Electrical and Information Engineering, Lanzhou University of Technology, China, in 2012. He is currently an Associate Professor in the College of Physics & Electromechanical Engineering at Hexi University, China. His research interests include prognostics, condition monitoring and fault diagnosis.

Lixiao Wu received her M.S. degree in mechanical engineering from the Gansu University of Technology, China, and the degrees from the School of Mechanical and Aerospace Engineering, Nanyang Technological University, Singapore, in 1998 and 2006, respectively. She is currently with the School of Mechanical and Electrical Engineering at Lanzhou University of Technology, China. Her research interests are in the area of chemical-mechanical polishing and contact mechanics.